Materials & Design 219 (2022) 110765

Contents lists available at ScienceDirect

Materials & Design

journal homepage: www.elsevier.com/locate/matdes

3D-printed bionic superhydrophobic surface with petal-like microstructures for droplet manipulation, oil-water separation, and drag reduction

Yang Liu, Hui Zhang *, Pu Wang, Zunyan He, Guangneng Dong

Key Laboratory of Education Ministry for Modern Design and Rotor-bearing System, Xi'an Jiaotong University, 28 Xianing West Road, Xi'an 710049, PR China

HIGHLIGHTS

- A 3D-printed biomimetic superhydrophobic surface with petal-like microstructures is proposed.
- Parameters of microstructure array are optimized to achieve high bearing capacity.
- Sharp edge effect combining with the arc curve effect is responsible for the super repellence property.
- Applications of the optimized petal-like microstructured surface are studied.

GRAPHICAL ABSTRACT

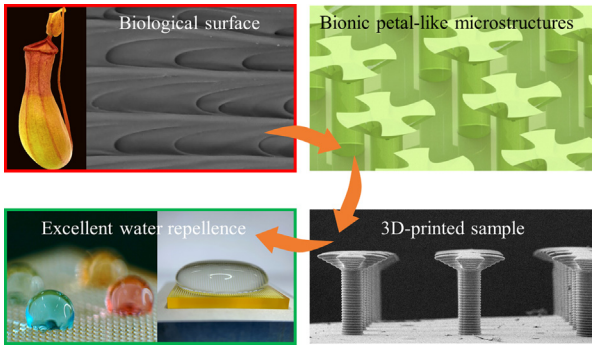

ARTICLE INFO

Article history:
Received 27 February 2022
Revised 12 May 2022
Accepted 18 May 2022
Available online 25 May 2022

Keywords:
Bionic
Petal-like microstructures
Superhydrophobic surface
Water repellence

ABSTRACT

Recently, bioinspired mushroom or reentrant mushroom microstructures have attracted intersts of researchers for their amazing water superrepellence property. However, basic principles of exquisite microstructures design for improving water repellence are still lacking. This paper reports a novel 3D-printed biomimetic superhydrophobic surface with petal-like microstructures inspired by the droplet pinning effect of nepenthes peristome. Then, parameters such as petal number, petal proportion and spacing distance are studied and optimized to improve water repellence, which is evaluated according to droplet bearing capacity. The results show that when the petal number is 4, the spacing distance is 100 μm, and the petal proportion is 50%, the petal-like structured surface achieves its maximum droplet bearing capacity. Comparing with the common mushroom microstructures, the maximum increase rate in bearing capacity is 58.3% for the optimized petal-like microstructures. Corresponding mechanism analysis attributes such superrepellence property to the sharp edge effect and the arch curve effect. Furthermore, the excellent water repellence enables the petal-like microstructured surface to be used for water droplets manipulation, oil-water separation, and captured-air drag reduction.

1. Introduction

In the past few years, functional surfaces with different wetting properties inspired by natural biology have flourished in fields ranging from water collection [1,2], droplet manipulation [3], fog collection [4], drag reduction [5] even to oil-water separation [3] and drug delivery systems [6]. Especially, water-repellent surfaces have attracted keen interests of researchers and become a hot topic [7–9]. Traditional methods to achieve the water-repellent property generally includes changing surface roughness, modifying chemical substance and their combination [10–12] to convert surface

* Corresponding author.
E-mail address: zhanghui7@xjtu.edu.cn (H. Zhang).

https://doi.org/10.1016/j.matdes.2022.110765

wettability from hydrophilic to superhydrophobic. However, lots of research experience shows that changing surface roughness only influences surface wettability in a limited range [13–15]. Chemical substance modification is an effective way to achieve superhydrophobic surface, but it may result in the problem of surface unstability [16,17] and toxicity [18,19].

Initially, researchers noticed that rose petal has the superhydrophobic property with contact angle (CA) larger than 150°, but it still adheres water droplet firmly (petal effect) [20,21], which is obviously different from the famous lotus effect. The mechanism is attributed to rose petal surface has unique micro/nano fractal structures, but it does not process any low surface energy coatings, such as wax which covers the whole surface of lotus leaves. This phenomenon indicates surfaces made of hydrophilic material with special microstructures or nanostructures may achieve superhydrophobicity. Based on this assumption and inspired by biological surfaces, an increasing number of researchers were devoted to designing and fabricating unique microstructures or nanostructures to make surfaces consisting of hydrophilic materials present superhydrophobic properties, thus achieving specific functions. Typically, Weisensee et al. [22] presented metallic micro-mushroom reentrant structures on steel over the centimeter-scale using micro-electrical discharge machining. The surface showed characterization of hydrophobicity and oleophobicity. Yin et al. [23] reported a microstructured mushroom-like surface fabricated through 3D printing technology inspired by springtail skin. Such surfaces exhibited superhydrophobic properties and could be used to manipulate droplets. Liu et al. [24] put forward 3D-printed micro doubly reentrant arrays to realize liquid adhesion. Then various arrays were designed to show tuning macro/micro liquid droplets manipulation. Kim et al. [25] demonstrated that robust omniphobic surfaces with mushroom-like reentrant structures had water repellent property. Liu et al. [26] designed a kind of triply reentrant structures via two-photon polymerization, possessing repellence to water and organic liquids. Chandramohan et al. [27] reported a mushroom-structured substrate acted as the cooled substrate, which was fabricated by photolithography and electroplating.

In addition to mushroom [22,25,27] or reentrant mushroom [24,26] microstructures as abovementioned, more and more other complex microstructures were proposed and fabricated with the development and maturity of micro 3D printing technology. Yang et al. [3] fabricated a kind of micrometer-scale artificial hairs with eggbeater heads inspired by Salvinia molesta leaf to achieve superhydrophobicity and petal effect. Then, an oil/water separation solution based on the structures was performed. Hu et al. [28] designed a set of surfaces with mesoscale heads and spring sets in analogy to the mushroom-like geometry on springtail cuticles, which achieved flexible interfacial structures to endure tribological friction robustly as well as to promote water repellency.

Although the above studies have proposed water repellent microstructures with various shapes, most of these shapes have mushroom-like forms. It is still a chanllenge to design exquisite 3D microstructures and to explore the mechanisms in-depth, thus further improving droplet repellence property. Recently, the research [29] on nepenthes revealed that the exquisite combination of the sharp edge and the arch curve of the microcavity in the peristome area of the nepenthes have a superstrong ability to pin the liquid on the curved structure, even overcoming gravity [30]. The above research may provide a new solution for preventing the spread of droplets and pinning liquid [31–35].

Herein we report a novel 3D-printed biomimetic superhydrophobic surface with petal-like microstructures inspired by the water pinning effect of nepenthes peristome. The hydrophilic resin with petal-like microstructure exhibited macroscopic superhydrophobic properties and excellent water droplet repellence. Then, parameters such as petal number, spacing distance between adjacent structures, and proportion of petal were studied and optimized for improving water droplet bearing capacity. Furthermore, the possible mechanism was explored and elucidated through the experiments and force analysis. Lastly, the applications of such microstructured surfaces for bearing large volumes of water, flexible droplet manipulation, oil-water separation and captured-air drag reduction were performed.

2. Results and discussion

2.1. Design and fabrication of petal-like microstructured surface

The petal-like microstructure is inspired by the peristome of nepenthes which consist of numerous arch-shaped microcavities (Fig. 1**a-c**). The existence of these arch-shaped microcavities with sharp tilt edges makes a droplet dripping onto the peristome spread unidirectional towards the outer edge of nepenthes, even overcomes gravity (inset in Fig. 1**a**). These arch-shaped microcavities provide sufficient restraint for liquid pinning in the opposite direction towards the outer edge of nepenthes [29]. Inspired by such liquid pinning effect, similar arch-shaped sharp edges are arranged in an annular array, thus constituting a petal-like microstructure (Fig. 1**e**). Since the petal-like microstructure has annular arch-shaped sharp edges to restrain water from spreading to any radial outside direction, water may keep a droplet shape and exhibit relatively high CA (inset in Fig. 1**e**). We adopt the bionic design idea and advanced projection micro stereolithography (PμSL) 3D printing technology to fabricate the petal-like microstructure arrays (see Experimental section and methods). The schematic demonstration of the processing of 3D printing is shown in Fig. 1**d**. The 3D models were built by Solidworks, as shown in Fig. 1**e**, where the petal-like microstructure arrays are arranged on a 2 mm thick plane. Since the photocurable resin has hydrophilic properties, the 3D printed flat(bare) surface presents CA of ∼55° with a water droplet of 5 μL (Fig. 1**f**). The 3D printed surface with pillar microstructure demonstrates hydrophobicity with CA ∼90° (Fig. 1**g**). However, 3D printed surface with the petal-like microstructure shows an obviously macroscopical superhydrophobic property with CA of ∼160° (Fig. 1**h**). Moreover, the water adheres to the surface even when the surface is upside down, indicating the property of petal effect (Fig. 1**i**).

A series of biomimetic surfaces with petal-like microstructures of different geometrical parameters were fabricated by PμSL 3D printing system. SEM images present the details of the petal-like microstructures, as shown in Fig. 2. Each microstructure is deposited by layers with a thickness of approximately 8 μm. The head of each petal-like structure is designed to be flat for bearing droplets. The side view image in Fig. 2**a** illustrates the constant parameters of each single petal-like microstructure: the maximum diameter of the petal-like microstructure D = 300 μm, the head height h = 60 μm, the tilt angle α = 30°; the diameter of support column d = 100 μm, and the height of support column H = 250 μm. The discontinuous arch shapes of the upper surface are derived from the microstructure of nepenthes peristome, as shown in Fig. 1**c** and Fig. 1**e**. According to the arch shape of nepenthes peristome, the governing equation of arch (the golden yellow curve in Fig. 2**c**) is written as Equation (1):

$$\frac{x^2}{\frac{D^2}{25}\cdot\cos^2\frac{\pi\cdot(1-K)}{P}}-\frac{y^2}{\frac{D^2}{21}\cdot\sin^2\frac{\pi\cdot(1-K)}{P}}=1 \tag{1}$$

(shown in **Figure S1** and **Equation S1** and **S2**). P is defined as the number of petals. S is the spacing distance between the two adjacent microstructures. K is defined as the ratio of arch length to circumference ($K = C'/C$), as shown in Fig. 2**c**. As shown in Fig. 2-

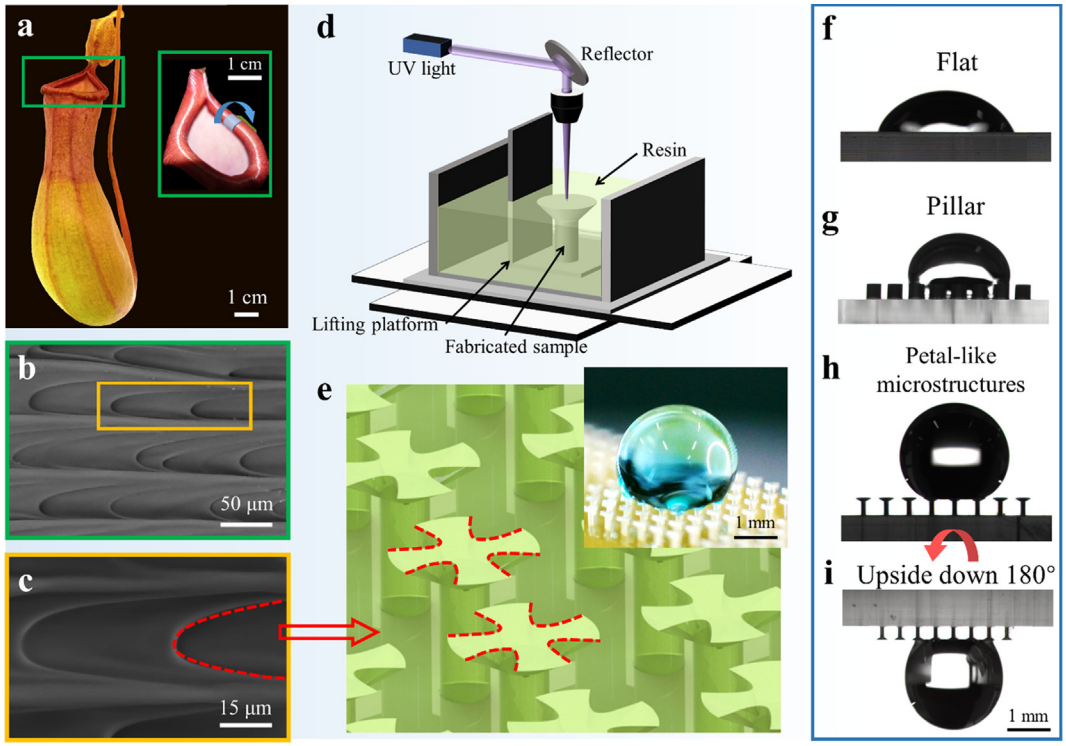

Fig. 1. Biomimetic 3D-printed petal-like microstructures. a Photograph of nepenthes, showing the directional water spreading behavior on the peristome. **b–c** SEM images of the peristome with numerous arch-shaped microcavities. **d** Schematic of the projection micro stereolithography (PμSL) 3D printing system. **e** 3D models of petal-like microstructures with arch-shaped sharp edges. **f** Water droplet on the 3D printed flat (bare) surface, presenting hydrophilicity with ~55° CA. **g** Water droplet on the 3D printed surface with pillar microstructures, presenting hydrophobic property with ~90° CA. **h-i** Water droplet on the 3D printed surface with petal-like microstructures presenting CA ~160° and it presents superior adherence even when the surface is upside down.

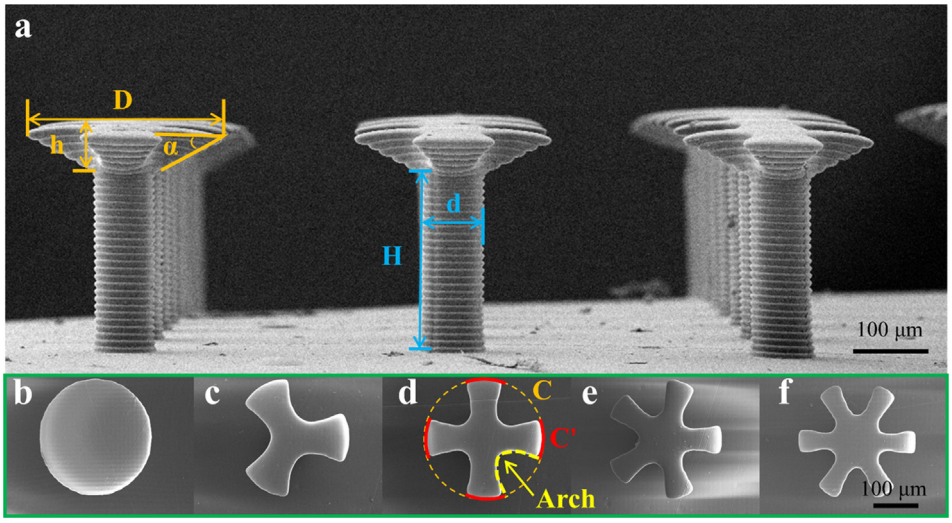

Fig. 2. SEM images of petal-like microstructures. a Side view of petal-like microstructures marked with geometrical parameters. **b-f** Top view of petal-like microstructure with different petal numbers of 0, 3, 4, 5, and 6.

b-f and **Table S1**, *K* and *S* are fixed to be 0.5 and 100 μm, respectively, while *P* is preassigned to be 0 (flat circular mushroom shape), 3, 4, 5, and 6. As shown in **Figure S2a** and **Table S2**, *K* and *P* are fixed to be 0.5 and 4, respectively, while *S* increases from 40 μm to 140 μm with an increment of 20 μm. As shown in **Figure S2b** and **Table S3**, *P* and *S* are fixed to be 4 and 100 μm, respectively, while *K* increases from 0.3 to 1 (flat circular mushroom shape) with an increment of 0.1.

2.2. Investigation of droplet bearing capacity

Experimental study on the effect of geometrical characters (*P*, *S* and *K*) on the droplet bearing capacity of petal-like microstructured surface were carried out in this section. Micro-droplets of 1 μL was dripped and added continuously to the tested surface with an 8 × 8 square array of petal-like microstructures by a micro-syringe until the droplet was collapsed. Curves of the num-

ber of microstructures covered by the droplet (shown in Fig. 3**a, c and e**) and the CA (shown in Fig. 3**b, d and f**) changing with droplet volume were plotted. Meanwhile, when the droplet collapsed, the volume of the water droplet was recorded as collapse volume and plotted as a bar chart (shown in Fig. 3**g**). The parameters of covered microstructure number, CA and collapse volume reflect the droplet carrying capacity.

Obviously, water droplets keep a spherical shape and stand on the petal-like microstructured surface, compared with its spreading or submerging on the plane surface and surface with pillar microstructures (Fig. 1**f** and **g**). As illustrated in Fig. 3**a**, before collapse, the occupied microstructure number for microstructures with 3 and 4 petals is less than those with 0 (mushroom shape), 5 and 6 petals. As shown in Fig. 3**a** and **g,** the collapse volume for microstructures with 3 and 4 petals is larger than those with 0, 5 and 6 petals. For example, for the surface with 0 petals microstructures, its collapse volume is 50 μL. However, the droplet on microstructures with 4 petals does not collapse until 76 μL. The CA presents a fluctuation trend varying with water volume for petal-like microstructured surfaces. Such fluctuation may be attributed to the number of microstructures covered by water jumps with continuous dripping and volume increase of the droplet. Comparing with the surface of the mushroom-shaped structure with 0 petals, surface with microstructures with 3 and 4 petals has larger CA. Hence, microstructures with 3 and 4 petals exhibit more significant water repellence and higher bearing capacity. Microstructures with 4 petals present the best load bearing capacity.

It should also noticed that since the existence of petal-like microstructures, the upper bearing surface is not a continuous plane. The number of microstructures covered by droplet increases with the increase of droplet volume. Hence, the CA and the contact angle hysteresis (CAH) on the discontinuous flat with the petal-like microstructures present different values comparing with droplets on complete plane (as shown in **Table S4**). In Fig. 3**b, 3d, and 3f**, the upward trends of polylines reflect the hysteresis phenomenon. For each upward polyline, the droplet expands with the increase of volume, but it covered a certain number of petal-like microstructures and the length of contact line kept to be constant. When the the droplet swell to cover more microstructures, the polyline of CA exhibits a sharp drop trend and then begin to increase as another cycle due to the hysteresis effect.

The effect of the spacing distance between adjacent microstructures S on droplet bearing capacity is presented in Fig. 3**c** and **g**. As shown in Fig. 3**c** and **g**, with the increase of S, the collapse volume exhibits an initial increase trend. But when S becomes larger than 100 μm (i.e. 120 μm and 140 μm), the collapse volume has a sudden drop. For microstructures with the S of 120 μm or 140 μm, the collapse volume is less than 10 μL. The curves of CA show that microstructures with S of 100 μm have bigger magnitude and more stable fluctuation than other microstructures, indicating higher energy barriers between adjacent microstructures, which may result in more significant water repellence and higher bearing capacity.

The ratio of arch length to circumference K reflects the occupation proportion of petals in the circumferential direction. When K is less than or equal to 0.4, the collapse volume is smaller than 4 μL, implying very weak and unstable droplet bearing capacity. When K increases to 0.5, the droplet collapse volume increases significantly. However, with further increase of K, the collapse volume exhibits a gradual decrease trend, which is presented in Fig. 3**e** and **g**.

Based on the above study, the optimized microstructure array with parameters: petal number P to be 4, spacing distance S to be 100 μm, and the ratio of arch length to circumference K to be 0.5 are obtained as the optimized microstructure. Comparing with the common mushroom microstructures, the maximum increase rate in bearing capacity is 58.3% for such petal-like microstructures.

2.3. Mechanism analysis

When a droplet is dripped onto the 3D-printed petal-like microstructured surface, it generally covers a square array of multiple microstructures (Fig. 4**a**). The droplet on the top plane of microstructures presents zigzag boundary, as illustrated in Fig. 4b. The synergy of the arch-shaped curve and the sharp edge of the petal-like structure act as energy barriers and generate constraint forces (as shown by red arrows) to restrict the spread of water droplets, no matter the droplet is in partial covering status or full covering status (Fig. 4**b**), thus increasing the CA to exhibit water repellence property. To confirm the sharp edge effect and arch curve effect, two fusiform blocks were fabricated through 3D-printing technology, as shown in Fig. 4**c**. Block-1 (length10 mm, width 3 mm, height 2 mm, shown in Fig. 4**c1**) has a straight sharp edge of 30° at one end, while at the other, the straight edge has a corner angle of 90°. Block-2 (length10 mm, width 3 mm, height 2 mm, shown in Fig. 4**c2**) has a convex arch edge with a corner angle of 90° at one end, while at the other, it has a concave arch with a corner angle of 90°. Before the experiment, two plexiglass sheets adhered to the lateral sides of the block. The block was suitably settled to guarantee its top surface was horizontal. Then, water droplets of 5 μL were dripped onto the top surface of the block continuously step by step until it collapsed at any end of the block. This process was observed and recorded by a high-speed camera. From Fig. 4**c1**, it is observed that with the continuous increase in volume of water droplet, droplet collapse occurres at the edge with a corner angle of 90°, indicating that the relatively sharper edge generates larger constraint force to restraint the spreading of water, while the right edge (of block or pillar) cannot provide enough force to hold the droplet when the volume of droplet is larger than a threshold (as the force analysis shown in **Figure S3**). This phenomenon is the so-called sharp edge effect. For the case where the liquid wet the edge of a solid, the CA of water droplet should be limited within the scope as shown in Expression (2) [29,30]. When the CA θ is smaller than the critical value θ_c, the water droplet could be pinned at the sharp edge.

$$\theta_0 \leqslant \theta \leqslant \theta_c = (180^\circ - \varphi) + \theta_0 \tag{2}$$

where θ_0 is the intrinsic CA of water droplets on the plane of the same material; φ is the corner angle of the edge.

Similarly, with the continuous increase in volume of water droplet, water collapse occurres at the convex arch shaped edge, thus demonstrating the arch curve effect, which could be described as the concave arch shape enhances the water restraint effect of the edge, while the convex arch shape weakens the water restraint effect for the edge, in Fig. 4**c2**. Since the petals have hydrophilic property, the droplet is streched along the petals forming concave liquid boundary curves (Fig. 4**d1**), similar to the situation of liquid in parallel sidewalls (Fig. 4**d2**). The similar shape of liquid boundary curve and the concave arch curve of sharp edges may result in relatively high water restraint force.

2.4. Applications of petal-like microstructure

The bioinspired petal-like microstructured surface has the application potential in a variety of engineering fields. Herein, a 20 mm × 20 mm surface composed of petal-like microstructures (P = 4, S = 100 μm, K = 0.5) was fabricated. Then, water droplets of 5 μL were dripped onto the top surface continuously. It was observed water droplet did not collapse with the increase of volume due to the superrepellence property brought by the

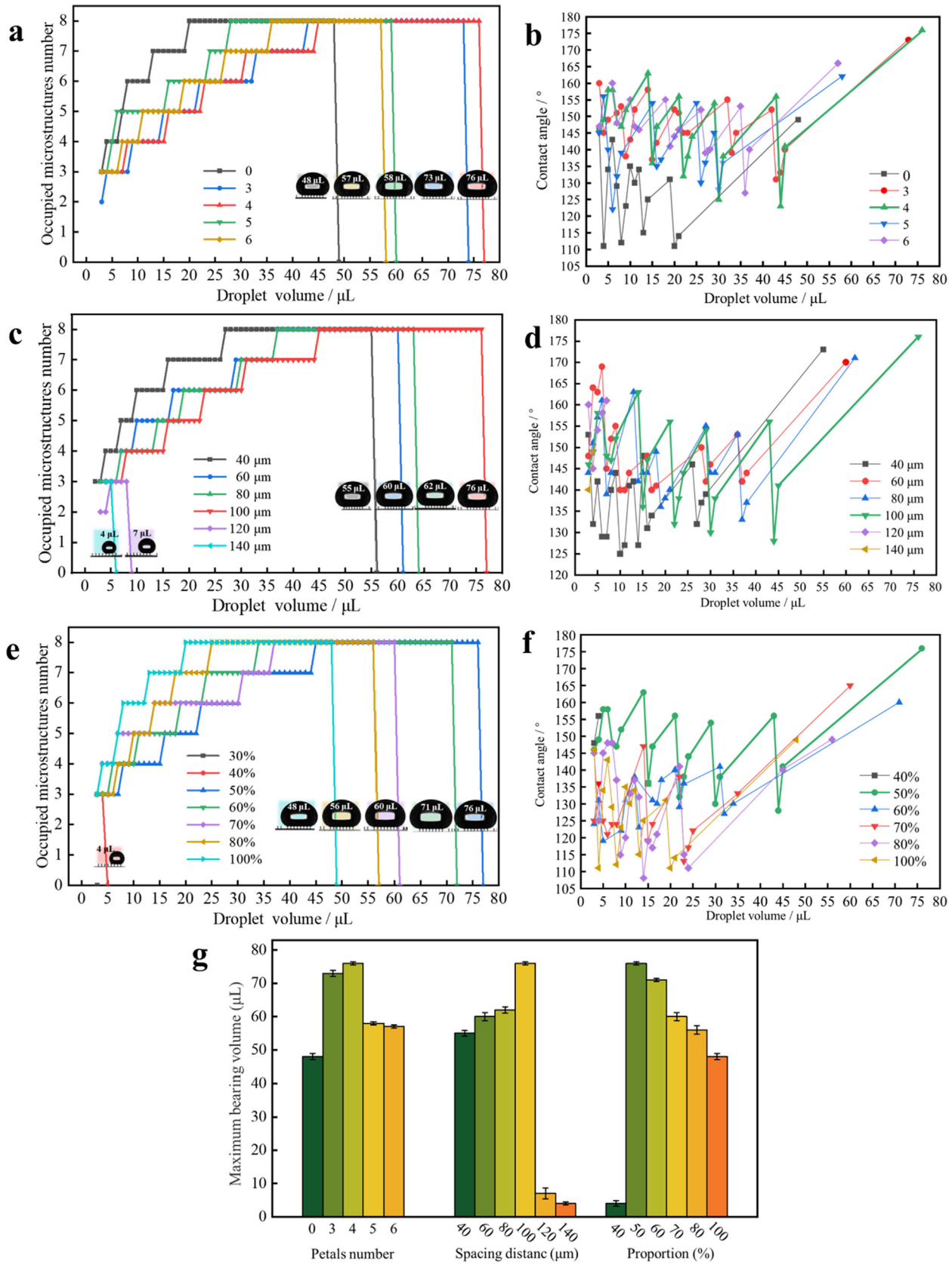

Fig. 3. Droplet bearing capacity for petal-like microstructures. a Occupied number of microstructures with different *P* varies with droplet volume. **b** CA changing with droplet volume on the petal-like microstructures with different *P*. **c** Occupied number of microstructures with different *S* varies with droplet volume. **d** CA changing with droplet volume on the petal-like microstructures with different *S*. **e** Occupied number of microstructures with different *K* varies with droplet volume. **f** CA changing with droplet volume on the petal-like microstructures with different *K*. **g** Maximum bearing volume of petal-like microstructure array with different geometrical parameters.

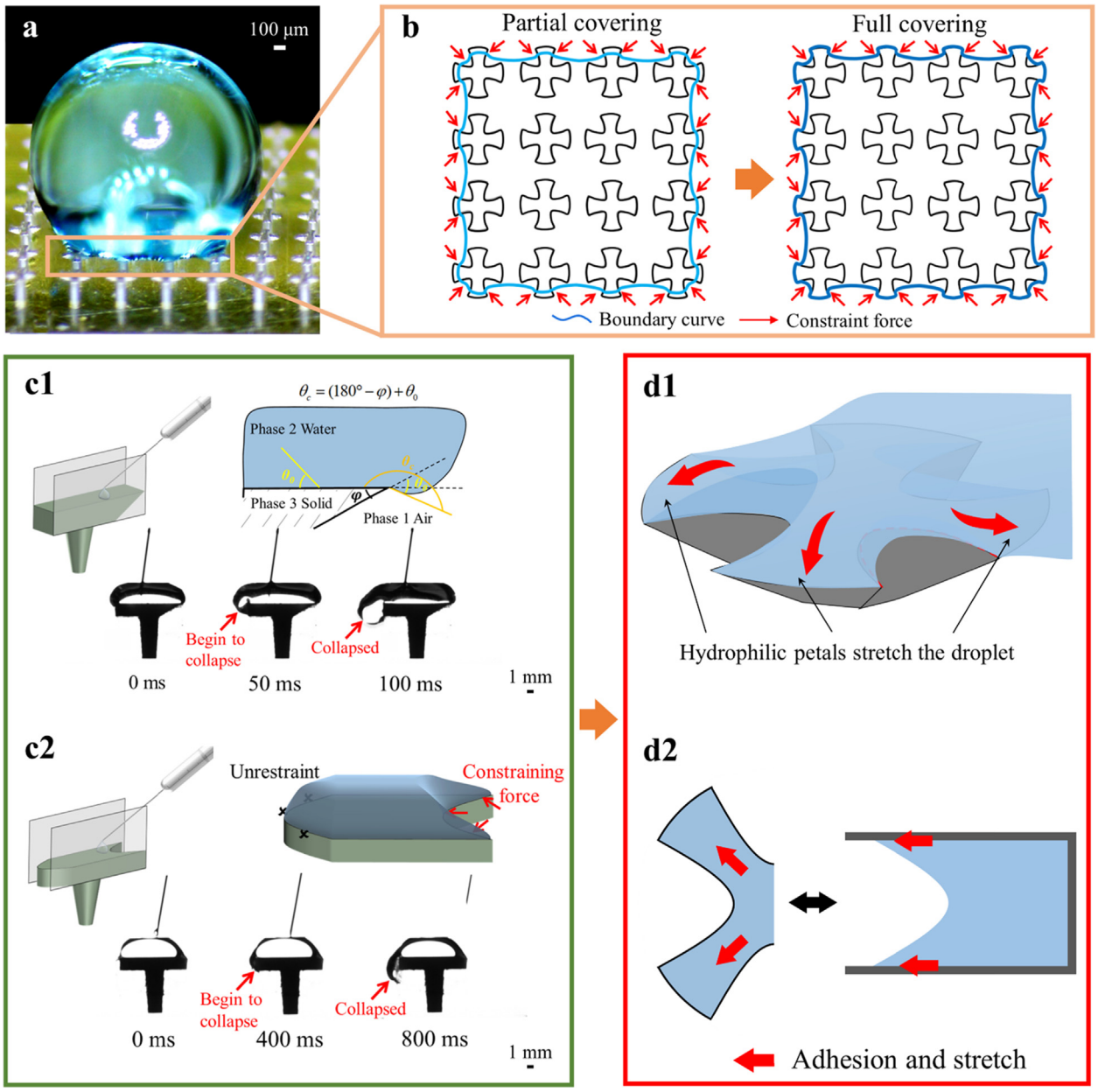

Fig. 4. Mechanism for droplet bearing capacity of petal-like microstructures. a Droplet stands on the top of the microstructure array and presents a zigzag boundary along the edge of microstructures. **b** Schematic illustration of the contact boundary between the droplet and the microstructure. **c1-2** Schematic of experiment to demonstrate the sharp edge effect and arch curve effect. **d1-2** Illustration of hydrophilic petals strech the droplet and the adhesion and streching effect of petal structures and parallel sidewalls.

microstructures. Finally, a droplet of large volume (3 mL) with an air cushion between it and the substrate (Cassie state) was formed, as shown in Fig. 5**a**.

A classical reaction between $FeCl_3$ and NaOH was carried out to demonstrate the superior droplet bearing capacity for various solutions working as a liquid-droplet-based micro-reactor. 1 mL dropper was used to instill droplets of various chemicals onto the surface of petal-like microstructure. A droplet of 10 μL 0.5 mol·L^{-1} $FeCl_3$ solution was firstly deposited onto the surface followed by the droplet of 3 μL 1 mol·L^{-1} NaOH solution. The droplet maintained the spherical shape and stably stayed on the surface during the whole reaction, shown in Fig. 5**b**. The coalescence of the two chemicals produced the brown flocculent precipitate suspended in spherical droplets due to the chemical reaction: $FeCl_3 + 3NaOH = Fe(OH)_3\downarrow + 3NaCl$, shown in the **Movie S1**. The chemical reaction that takes place in the form of spherical droplets on the surface of the petal-like microstructures, on the one hand, saves materials and helps to observe the reaction phenomenon and adjust the corresponding concentration in time; on the other hand, is convenient for the manipulation of the reacted droplets and the substances in them.

Petal-like microstructure arrays with different geometrical parameters of *P*, *S* and *K* exhibit discrepancy in droplet adhesion ability, which may be used for droplet manipulation. An experiment on lossless droplet manipulation was carried out. Firstly, a water droplet of 5 μL was dripped on a microstructured surface with relatively low density (P = 4, S = 120 μm, K = 0.5) array. Then, a microstructured surface with medium density (P = 4, S = 100 μm, K = 0.5) array was used to grab the droplet on the low density microstructured surface, and released it down on a surface with

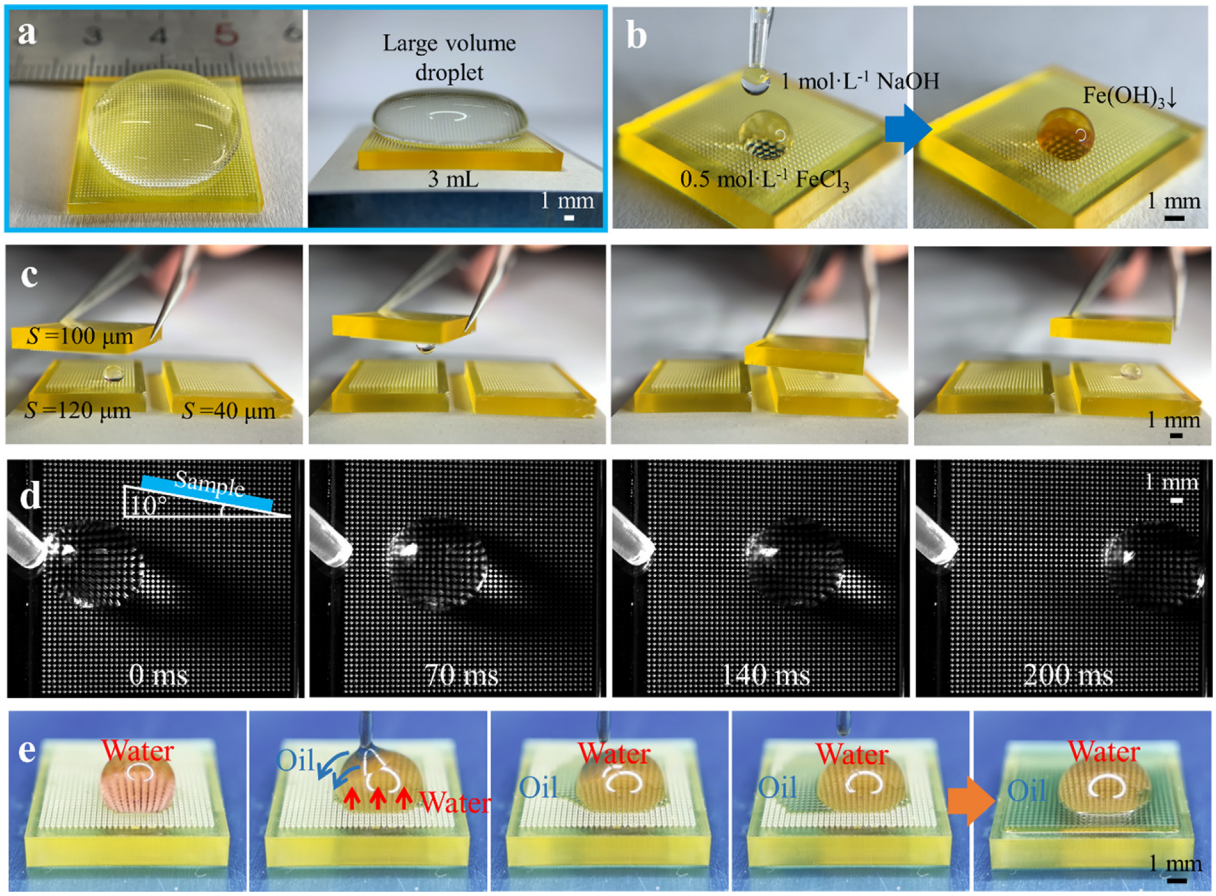

Fig. 5. Applications of the petal-like microstructured surface. a 20 × 20 mm surface composed of petal-like microstructures for bearing large water droplets. **b** Chemical reaction of a 0.5 mol·L^{-1} $FeCl_3$ droplet with a 1 mol·L^{-1} NaOH droplet on the petal-like microstructures. **c** Lossless water droplet manipulation between petal-like microstructures of diverse parameters. **d** Rapid sliding of water droplets on inclined surfaces composed of petal-like microstructures. **e** Oil-water separation.

high density (P = 4, S = 40 μm, K = 0.5) arrays, shown in Fig. 5**c** and **Movie S2**. When the gap of array density between two surfaces is relatively large, dense array implies that more microstructures are in contact with the droplet, thus generating higher adhesion force than sparse array. When the gap of array density between two surfaces is relatively small, relatively dense array implies the locations of contacted microstructures are closer to the middle of the droplet, thus also having higher adhesion force than the relatively sparse array, as shown by the high-speed microphotographs in **Figure S4** and **Movie S3**. It is also observed that almost no residual was left on the petal-like microstructures, thus demonstrating that the droplet manipulation process was no weight loss.

Comparing with mushroom shapes, petal-like microstructures exhibit excellent water repellence property, and meanwhile keep relatively small contact areas with water droplet. Hence, the adhesion force between water droplet and petal-like microstructured surface is smaller than droplets on mushroom-shaped structures. Such small adhesion force even cannot fix big droplets when the surface tilts at an angle. A water droplet of ~ 300 μL was released on the microstructured surface tilted with an angle of 10°, as shown in Fig. 5**d** and **Movie S4 and S5**. The water droplet quickly sliding down along the surface with no weight loss. The movement of the droplet is driven by the component force (along the inclined surface) of gravity $F_c = mg\sin\delta$ and is resisted by the dissipative forces $F_d = k \cdot 2R \cdot \gamma \cdot (\cos\theta_r - \cos\theta_f)$ [36–38], where m is droplet mass, g is gravitational acceleration, δ is the tilt angle of the surface, k is the dimensionless parameter and assumed to be 1, R is the radius of droplet, γ is water/air surface tension, θ_r and θ_f represents the apparent rear and front contact angles of droplet, respectively. When a 300 μL droplet was released on the 10° inclined surface, the snapshots were recorded by a high speed camera. The component force of gravity along the 10° inclined surface F_c is calculated to be ~475 μN. From the snapshots, θ_r and θ_f can be measured, which facilitate the calculation of F_d. Since the values of θ_r and θ_f are different for different snapshots, F_d has a fluctuation range to be ~361 ± 47 μN, as shown in **Fig. S5-6**. Obviously, the dissipative forces F_d was lower than the driving force F_c. (as shown in Fig. S5-6). This experiment demonstrates that hydrophilic material with such special petal-like microstructures can also present the lotus effect.

Environmental protection and green economy have increasingly demanded effective oil-water separation. Some previous researches have mainly focused on nanomaterials with multilayer complex structures or special chemical properties which require complex synthesis processes [39–41]. Since oil and water have different surface tensions, bearing capacity of the petal-like microstructures for oil and water are different, which may be used for the oil-water separation. As shown in Fig. 5**e** and **Movie S6**, a water droplet was placed on the petal-like microstructures. Then, a droplet of white mineral oil was dipped onto the top of the spherical water droplet. The oil droplet slid down along the surface of the water droplet and was quickly immersed into the petal-like microstructures while the water droplet kept the spherical shape, as shown in Fig. 5**e** and **Movie S6**.

The petal-like microstructure array surrounded by walls with sharp edge at inner side was used for bubble reserving and drag

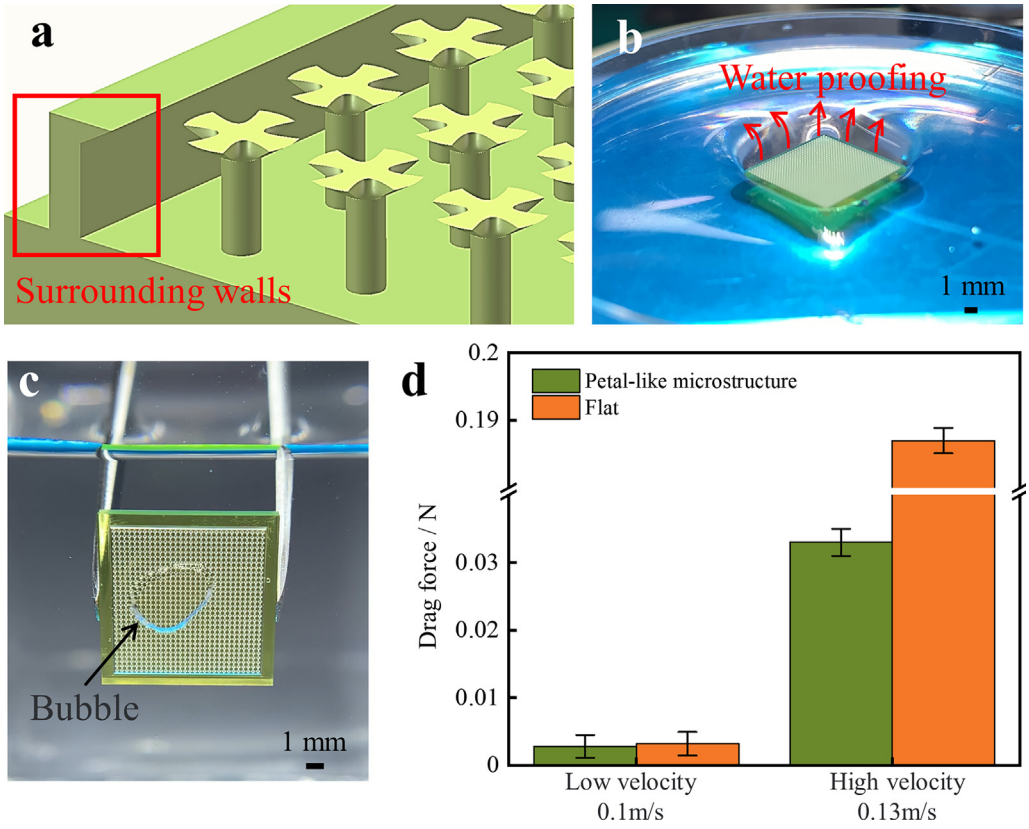

Fig. 6. Drag reduction effect of petal-like microstructures. a Petal-like microstructured surface with surrounding walls. **b** Water proofing effect of microstructured surface. **c** Captured air bubble by petal-like microstructures under water. **d** Bar chart of drag force for flat and microstructured surfaces.

reduction as shown in Fig. 6**a**. Water was injected continuously into a petri dish, where a sample with petal-like microstructured surface as shown in Fig. 6**a** adhered to the bottom of the petri dish. The sample exhibited excellent waterproofing properties due to the existence of petal-like microstructures and surrounding walls with sharp edge, as shown in Fig. 6**b**. When the sample was put under water, a bubble was captured inside the microstructures, as shown in Fig. 6**c** and **Movie S7**. It is observed that a bubble was captured firmly although the volume of bubble was changing due to the changing of water pressure with the depth. The drag force of such microstructured surface was tested using a drag monitor device (shown in **Figure S7**). The surface and the sensor were combined by a bracket (l = 100 mm). The torque of drag resistance T_z was directly measured by a six-axis force sensor. And drag force F_z was calculated by $F_z = T_z / l$. Two flow velocity were selected for the experiment: 0.13 m/s (high velocity) and 0.1 m/s (low velocity). The result of drag force (shown in Fig. 6**d**) shows that comparing with flat surface, the petal-like microstructured surface has a significant reduction effect on drag force, especially for relatively high velocity. The possible mechanism is attributed to the bubble separating the solid surface and water, which may cause boundary slip effect to reduce fluid drag [42,43].

3. Conclusion

A 3D printing biomimetic superhydrophobic surface with petal-like microstructures inspired by the water pinning effect of nepenthes peristome is proposed. Parameters such as petal number, spacing distance and petal proportion are studied and optimized for enhancing water droplet bearing capacity. Microstructure array with parameters: petal number to be 4, the spacing distance to be 100 μm, and ratio of arch length to circumference to be 0.5 are obtained as the optimized structure. Comparing with common mushroom microstructure, the maximum increase rate in bearing capacity is 58.3% for the optimized petal-like microstructure. Corresponding mechanism analysis reveals that the sharp edge effect and the arch curve effect are responsible for such super repellence property. Possible applications of the optimized petal-like microstructured surface are studied. Experiments show the surface with petal-like microstructures exhibits excellent water repellence and could be used for droplets manipulation, oil-water separation, and captured-air drag reduction. Additionally, such water repellence property may make the microsturctured surface to be used in many other advanced fields, such as delaying biofilm formation [35].

4. Experimental section and methods

4.1. Fabrication of petal-like microstructures

The arrays of petal-like microstructures were fabricated by projection micro stereolithography (PμSL) 3D printing system –BMF-P140 (BMF Material Technology Inc., China). The maximum projection area of the 3D printing system could reach 20 mm × 20 mm, while the minimum printing layer thick is 5 μm. The wavelength of UV LED illuminant is 405 nm. The 3D models were built by Solidworks. The 3D structures are projected layer by layer onto the fluid resin using a high-precision ultraviolet lithography projection system. A layer gets to solidify in the exposed area in a few seconds and the translational projection stage lowers down to prepare for the next step. With accumulation of layers, a 3D sample is finally formed from the digital model. The 3D fusiform blocks were fabricated through another 3D printer (M-Jewelry U50, MakeX, China).

4.2. Test of droplet bearing performance

The droplet bearing capacity experiments and the CA measurements were carried out on the measuring device (OCA20, Dataphysics Co., Germany). The sample was placed on the platform of the measuring device. Water droplets were deposited onto the top of the arrays of petal-like microstructures by a microsyringe with a resolution of 1 μL.

4.3. Image acquisition

SEM images showing the morphology features of the peristome and the parameters of single petal-like microstructure were taken by field emission scanning electron microscope (GIMINI 500, ZEISS, Germany). The photographs and videos of nepenthes and water droplets of 3 mL, the reaction between $FeCl_3$ and NaOH, droplets manipulation and oil–water separation on the petal-like microstructures were taken by the optical camera (5D Mark Ⅱ, Canon, Japan). The collapse of droplets on the 3D fusiform blocks and the rolling down of droplets on the tilt surface were observed by a high-speed camera (AZ Instruments Cooperation, AZ9501, Taiwan China).

4.4. Experiment of drag reduction effect

In order to measure the drag reduction performance, a low Reynolds number circulating water test bench was built. The measuring device with the sample were suspended by an aluminum frame so that the sample was in the center of the tank. The surface and the sensor were combined by a bracket (l = 100 mm) fabricated through the 3D printer (M-Jewelry U50, MakeX, China). The torque of drag resistance was measured by a six-axis force sensor (Mini 40, ATI, USA). The data of torque is collected through the multi-dimensional mechanical signal acquisition device.

5. Supporting information

Hyperbola governing equation of petal-like microstructures; top view SEM images of petal-like microstructures with different *S* and *K;* table of structural parameters of petal-like microstructure with different *P, S* and *K;* table of CA and CAH on various number on various petal-like microstructure; force analysis of the sharp edge effect, the snapshots of grabbing a droplet using the petal-like microstructured surfaces; snapshots of water droplets sliding along the inclined surface consisting of petal-like microstructures; calculated component force (along the inclined surface) of gravity F_c and dissipative forces F_d and schematic of circulating water test bench. (PDF)

Chemical reaction of $FeCl_3$ with NaOH on the petal-like microstructures. (MP4)

Lossless water droplet manipulation. (MP4)

Grabbing a droplet using petal-like microstructured surfaces. (MP4)

Rapid sliding of water droplets on inclined surfaces with petal-like microstructures. (MP4)

Oil-water separation. (MP4)

Captured air bubble by petal-like microstructures under water. (MP4)

Author Contributions

The manuscript was written through contributions of all authors. All authors have given approval to the final version of the manuscript.

Funding Sources

This study was funded by National Natural Science Foundation of China (No. 52075418 and No. 51705400), China Postdoctoral Science Foundation (No. 2017M610633 and No. 2019T120896), and Postdoctoral Science Foundation of Shaanxi Province (2017BSHEDZZ153).

Declaration of Competing Interest

The authors declare that they have no known competing financial interests or personal relationships that could have appeared to influence the work reported in this paper.

Appendix A. Supplementary data

Hyperbola governing equation of petal-like microstructures; top view SEM images of petal-like microstructures with different *S* and *K*; table of structural parameters of petal-like microstructure with different *P, S* and *K*; table of CA and CAH on various number on various petal-like microstructure; force analysis of the sharp edge effect, the snapshots of grabbing a droplet using the petal-like microstructured surfaces; snapshots of water droplets sliding along the inclined surface consisting of petal-like microstructures; calculated component force (along the inclined surface) of gravity F_c and dissipative forces F_d and schematic of circulating water test bench (PDF). Chemical reaction of $FeCl_3$ with NaOH on the petal-like microstructures. (MP4) Lossless water droplet manipulation. (MP4). Grabbing a droplet using petal-like micro structured surfaces. (MP4). Rapid sliding of water droplets on inclined surfaces with petal-like microstructures. (MP4). Oil-water separation. (MP4). Captured air bubble by petal-like microstructures under water. (MP4). Supplementary data to this article can be found online at https://doi.org/10.1016/j.matdes.2022.110765.

References

[1] X. Liang, D. Li, ShanPeng Li, C. Xu, Z. Guo, Artificial Leaf for Switchable Droplet Manipulation, Langmuir 37 (18) (2021) 5745–5752, https://doi.org/10.1021/acs.langmuir.1c0079910.1021/acs.langmuir.1c00799.s001.

[2] H. Bai, L. Wang, J. Ju, R. Sun, Y. Zheng, L. Jiang, Efficient Water Collection on Integrative Bioinspired Surfaces with Star-Shaped Wettability Patterns, Adv. Mater. 26 (29) (2014) 5025–5030, https://doi.org/10.1002/adma.201400262.

[3] Y. Yang, X. Li, X. Zheng, Z. Chen, Q. Zhou, Y. Chen, 3D-Printed Biomimetic Super-Hydrophobic Structure for Microdroplet Manipulation and Oil/Water Separation, Adv. Mater. 30 (9) (2018) 1704912, https://doi.org/10.1002/adma.v30.910.1002/adma.201704912.

[4] L. Liu, S. Liu, M. Schelp, X. Chen, Rapid 3D Printing of Bioinspired Hybrid Structures for High-Efficiency Fog Collection and Water Transportation, Acs Applied Materials & Interfaces 13 (24) (2021) 29122–29129, https://doi.org/10.1021/acsami.1c05745.

[5] Y.-L. Zhang, H. Xia, E. Kim, H.-B. Sun, Recent developments in superhydrophobic surfaces with unique structural and functional properties, Soft Matter 8 (44) (2012) 11217–11231, https://doi.org/10.1039/c2sm26517f.

[6] C. Alvarez-Lorenzo, A. Concheiro, Smart drug delivery systems: from fundamentals to the clinic, Chem. Commun. 50 (58) (2014) 7743–7765, https://doi.org/10.1039/c4cc01429d.

[7] X. Su, H. Li, X. Lai, L. Zhang, X. Liao, J. Wang, Z. Chen, J. He, X. Zeng, Dual-Functional Superhydrophobic Textiles with Asymmetric Roll-Down/Pinned States for Water Droplet Transportation and Oil-Water Separation, ACS Appl. Mater. Interfaces 10 (4) (2018) 4213–4221, https://doi.org/10.1021/acsami.7b15909.

[8] X. Tang, P. Zhu, Y. Tian, X. Zhou, T. Kong, L. Wang, Mechano-regulated surface for manipulating liquid droplets, Nat Commun 8 (2017) 14831, https://doi.org/10.1038/ncomms14831.

[9] Y.M. Zheng, H. Bai, Z.B. Huang, X.L. Tian, F.Q. Nie, Y. Zhao, J. Zhai, L. Jiang, Directional water collection on wetted spider silk, Nature 463 (7281) (2010) 640–643, https://doi.org/10.1038/nature08729.

[10] H. Zhang, Y. Liu, M. Hua, G.-N. Dong, A Laser Scanning Method to Control the Location, Shape, Contact Angle and Sliding of Water Droplet on Superhydrophobic Surface, Adv. Eng. Mater. 21 (7) (2019) 1801375, https://doi.org/10.1002/adem.v21.710.1002/adem.201801375.

[11] H. Zhang, Y. Liu, Z. Zhang, M. Hua, G. Dong, A superhydrophobic surface patterned with hydrophilic channels for directional sliding control and manipulation of droplets, Surf. Coat. Technol. 409 (2021) 126836, https://doi.org/10.1016/j.surfcoat.2021.126836.
[12] D. Hu, Q. Yu, Y. Yang, L. Weng, Fabrication and wetting behaviour of micro/nanostructured mushroom-shaped silver pillar surface, Nanotechnology 31 (17) (2020) 175701, https://doi.org/10.1088/1361-6528/ab674b.
[13] Z. Zhu, S. Zheng, S. Peng, Y. Zhao, Y.e. Tian, Superlyophilic Interfaces and Their Applications, Adv. Mater. 29 (45) (2017) 1703120, https://doi.org/10.1002/adma.201703120.
[14] M. Liu, S. Wang, L. Jiang, Nature-inspired superwettability systems, Nat. Rev. Mater. 2 (7) (2017), https://doi.org/10.1038/natrevmats.2017.36.
[15] H. Zhang, M. Hua, G.N. Dong, D.Y. Zhang, K.S. Chin, A mixed lubrication model for studying tribological behaviors of surface texturing, Tribol. Int. 93 (2016) 583–592, https://doi.org/10.1016/j.triboint.2015.03.027.
[16] X. Tian, T. Verho, R.H.A. Ras, Moving superhydrophobic surfaces toward real-world applications, Science 352 (6282) (2016) 142–143, https://doi.org/10.1126/science.aaf2073.
[17] D. Wang, Q. Sun, M.J. Hokkanen, C. Zhang, F.-Y. Lin, Q. Liu, S.-P. Zhu, T. Zhou, Q. Chang, B.o. He, Q. Zhou, L. Chen, Z. Wang, R.H.A. Ras, X.u. Deng, Design of robust superhydrophobic surfaces, Nature 582 (7810) (2020) 55–59, https://doi.org/10.1038/s41586-020-2331-8.
[18] A. Elsaesser, C.V. Howard, Toxicology of nanoparticles, Adv. Drug Deliv. Rev. 64 (2) (2012) 129–137, https://doi.org/10.1016/j.addr.2011.09.001.
[19] W. Guo, Z. Li, Z. Ma, Review of Non-Fluorinated Durable Water Repellent and Stain-Resistant Materials and Their Future development, J. Phys. Conf. Ser. 1904 (1) (2021) 012010, https://doi.org/10.1088/1742-6596/1904/1/012010.
[20] L. Feng, Y. Zhang, J. Xi, Y. Zhu, N. Wang, F. Xia, L. Jiang, Petal effect: A superhydrophobic state with high adhesive force, Langmuir 24 (8) (2008) 4114–4119, https://doi.org/10.1021/la703821h.
[21] F. Xia, L. Jiang, Bio-inspired, smart, multiscale interfacial materials, Adv. Mater. 20 (15) (2008) 2842–2858, https://doi.org/10.1002/adma.200800836.
[22] P.B. Weisensee, E.J. Torrealba, M. Raleigh, A.M. Jacobi, W.P. King, Hydrophobic and oleophobic re-entrant steel microstructures fabricated using micro electrical discharge machining, J. Micromechanics Microengineering 24 (9) (2014) 095020, https://doi.org/10.1088/0960-1317/24/9/095020.
[23] Q. Yin, Q. Guo, Z. Wang, Y. Chen, H. Duan, P. Cheng, 3D-Printed Bioinspired Cassie-Baxter Wettability for Controllable Microdroplet Manipulation, ACS Appl. Mater. Interfaces 13 (1) (2021) 1979–1987, https://doi.org/10.1021/acsami.0c18952.
[24] X. Liu, H. Gu, H. Ding, X. Du, Z. He, L. Sun, J. Liao, P. Xiao, Z. Gu, Programmable Liquid Adhesion on Bio-Inspired Re-Entrant Structures, Small 15 (35) (2019) 1902360, https://doi.org/10.1002/smll.v15.3510.1002/smll.201902360.
[25] D.H. Kim, S. Kim, S.R. Park, N.X. Fang, Y.T. Cho, Shape-Deformed Mushroom-like Reentrant Structures for Robust Liquid-Repellent Surfaces, ACS Appl. Mater. Interfaces 13 (28) (2021) 33618–33626, https://doi.org/10.1021/acsami.1c0628610.1021/acsami.1c06286.s001.
[26] X. Liu, H. Gu, M. Wang, X. Du, B. Gao, A. Elbaz, L. Sun, J. Liao, P. Xiao, Z. Gu, 3D Printing of Bioinspired Liquid Superrepellent Structures, Adv. Mater. 30 (22) (2018) 1800103, https://doi.org/10.1002/adma.v30.2210.1002/adma.201800103.
[27] A. Chandramohan, S. Dash, J.A. Weibel, X. Chen, S.V. Garimella, Marangoni Convection in Evaporating Organic Liquid Droplets on a Nonwetting Substrate, Langmuir 32 (19) (2016) 4729–4735, https://doi.org/10.1021/acs.langmuir.6b00307.
[28] S. Hu, T. Reddyhoff, J. Li, X. Cao, X.i. Shi, Z. Peng, A.J. deMello, D. Dini, Biomimetic Water-Repelling Surfaces with Robustly Flexible Structures, ACS Appl. Mater. Interfaces 13 (26) (2021) 31310–31319, https://doi.org/10.1021/acsami.1c10157.
[29] H. Chen, P. Zhang, L. Zhang, H. Liu, Y. Jiang, D. Zhang, Z. Han, L. Jiang, Continuous directional water transport on the peristome surface of Nepenthes alata, Nature 532 (7597) (2016) 85–89, https://doi.org/10.1038/nature17189.
[30] J.F. Oliver, C. Huh, S.G. Mason, Resistance to Spreading of Liquids by Sharp Edges, J. Colloid Interface Sci. 59 (3) (1977) 568–581, https://doi.org/10.1016/0021-9797(77)90052-2.
[31] P. Zhang, L. Zhang, H. Chen, Z. Dong, D. Zhang, Surfaces Inspired by the Nepenthes Peristome for Unidirectional Liquid Transport, Adv. Mater. 29 (45) (2017) 1702995, https://doi.org/10.1002/adma.201702995.
[32] H. Chen, L. Zhang, P. Zhang, D. Zhang, Z. Han, L. Jiang, A Novel Bioinspired Continuous Unidirectional Liquid Spreading Surface Structure from the Peristome Surface of Nepenthes alata, Small 13 (4) (2017) 1601676, https://doi.org/10.1002/smll.v13.410.1002/smll.201601676.
[33] J. Li, X. Zhou, J. Li, L. Che, J. Yao, G. McHale, M.K. Chaudhury, Z. Wang, Topological liquid diode. *Science*, Advances 3 (2017) 10, https://doi.org/10.1126/sciadv.aao3530.
[34] X. Li, J. Li, G. Dong, Bioinspired Topological Surface for Directional Oil Lubrication, ACS Appl. Mater. Interfaces 12 (4) (2020) 5113–5119, https://doi.org/10.1021/acsami.9b20345.
[35] Y. Cao, S. Jana, L. Bowen, X. Tan, H. Liu, N. Rostami, J. Brown, N.S. Jakubovics, J. Chen, Hierarchical Rose Petal Surfaces Delay the Early-Stage Bacterial Biofilm Growth, Langmuir 35 (45) (2019) 14670–14680, https://doi.org/10.1021/acs.langmuir.9b02367.
[36] Y. Cao, S. Jana, X. Tan, L. Bowen, Y. Zhu, J. Dawson, R. Han, J. Exton, H. Liu, G. McHale, N.S. Jakubovics, J. Chen, Antiwetting and Antifouling Performances of Different Lubricant-Infused Slippery Surfaces, Langmuir 36 (45) (2020) 13396–13407, https://doi.org/10.1021/acs.langmuir.0c00411.
[37] N. Gao, F. Geyer, D.W. Pilat, S. Wooh, D. Vollmer, H.-J. Butt, R. Berger, How drops start sliding over solid surfaces, Nat. Phys. 14 (2) (2018) 191–196.
[38] D. Daniel, J.V.I. Timonen, R.P. Li, S.J. Velling, M.J. Kreder, A. Tetreault, J. Aizenberg, Origins of Extreme Liquid Repellency on Structured, Flat, and Lubricated Hydrophobic Surfaces, Phys. Rev. Lett. 120 (24) (2018), https://doi.org/10.1103/PhysRevLett.120.244503.
[39] R.K. Gupta, G.J. Dunderdale, M.W. England, A. Hozumi, Oil/water separation techniques: a review of recent progresses and future directions, J. Mater. Chem. A 5 (31) (2017) 16025–16058, https://doi.org/10.1039/c7ta02070h.
[40] T. Yu, G. Xu, X. Wang, J. Yang, J. Hu, Fabrication of Oil-Water Separation Filter Paper by Simple Impregnation with Fluorinated Poly-Acrylate Emulsion, Bioresources 9 (3) (2014) 4421–4429.
[41] Z. Xu, D. Jiang, Z. Wei, J. Chen, J. Jing, Fabrication of superhydrophobic nano-aluminum films on stainless steel meshes by electrophoretic deposition for oil-water separation, Appl. Surf. Sci. 427 (2018) 253–261, https://doi.org/10.1016/j.apsusc.2017.08.189.
[42] B. Bgpa, A. Gty, A. Kyk, B. Kska, The effects of microbubbles on skin friction in a turbulent boundary layer flow, Int. J. Multiphase Flow 80 (2016) 164–175.
[43] P. Du, J. Wen, Z. Zhang, D. Song, A. Ouahsine, H. Hu, Maintenance of air layer and drag reduction on superhydrophobic surface, Ocean Eng. 130 (jan.15) (2017) 328–335.